Journal Pre-proof

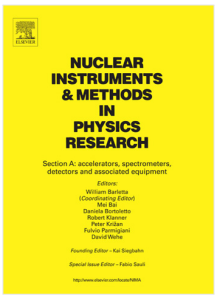

Multi-slice Energy Resolving CT system using a THCOBRA detector operating in $NeCH_4$

L.F.N.D. Carramate, A.L.M. Silva, C.D.R. Azevedo, S. De Francesco, A.M. da Silva, J.F.C.A. Veloso

PII: S0168-9002(19)31200-8
DOI: https://doi.org/10.1016/j.nima.2019.162738
Reference: NIMA 162738

To appear in: *Nuclear Inst. and Methods in Physics Research, A*

Received date : 26 January 2018
Revised date : 2 August 2019
Accepted date : 8 September 2019

Please cite this article as: L.F.N.D. Carramate, A.L.M. Silva, C.D.R. Azevedo et al., Multi-slice Energy Resolving CT system using a THCOBRA detector operating in $NeCH_4$, *Nuclear Inst. and Methods in Physics Research, A* (2019), doi: https://doi.org/10.1016/j.nima.2019.162738.

Multi-slice Energy Resolving CT system using a THCOBRA detector operating in $NeCH_4$

L. F. N. D. Carramate[a,*], A. L. M. Silva[a], C. D. R. Azevedo[a], S. De Francesco[b], A. M. da Silva[c], J. F. C. A. Veloso[a]

[a] *I3N, Physics Department, University of Aveiro, 3810-193 fi Aveiro, Portugal*
[b] *ESSUA, University of Aveiro, 3810-193 fi Aveiro, Portugal*
[c] *DETI/IEETA, University of Aveiro, 3810-193 fi Aveiro, Portugal*

Abstract

A 2D-Thick-COBRA based detector with 10×10 cm^2 active area operating in Ne/CH_4 (95/5) flow mode, was applied to X-ray Computed Tomography (CT). The CT system is based on a third generation scanner with the object motion provided by a stepper motor. Multi-slice acquisitions of a Poly(methyl methacrylate) phantom and of a sea snail were done and the cross-sectional images were used to perform tri-dimensional (3D) visualization of the objects. Both kind of images (cross-sectional and 3D) are presented. Cross-sectional images using energy intervals of the spectrum are shown. Also, a simulation study of the influence of discharges (intrinsic to the MicroPatterned Gaseous Detector operation) in the resulting cross-sectional image was done and presented, showing no significant influence on the final image.

Keywords: X-ray detectors, Thick-COBRA, Micropattern gaseous detectors, Computerized Tomography(CT)

1. Introduction

X-ray imaging has assumed a very important role in several fields of science, health care and industry. Particularly, imaging through Computed Tomography (CT) revolutionized medical care, is crucial in biomedical research and in several other applications such as archaeology, forensic science and industry quality control [1].

*Corresponding author
Email address: laracarramate@ua.pt (L. F. N. D. Carramate)

A CT system allows acquiring cross-sectional images and compute 3D images of the human body. Comparatively to a conventional X-ray image, CT allows visualizing the different structures and organs inside human body without superposition and provides higher contrast resolution, overcoming the limitations of conventional radiology [1, 2]. Recent developments in the detection subsystem that intend to use spectroscopic detectors are enabling a plethora of new imaging possibilities, as for example, contrast-to-noise ratio (CNR) improvement and/or dose decrease by applying the Energy Weighting Technique (EWT) [3, 4].

The EWT was applied in experimental CT data from different systems, achieving a CNR improvement of 40% with a cadmium zinc telluride detector [5] and 31% using the MicroHole & Strip Plate (MHSP) [6].

Generally, MicroPatterned Gaseous Detectors (MPGD) present nowadays a good solution for X-ray imaging and high energy physics experiments. They distinguish due to some interesting characteristics. These devices do not have dead areas, allowing a full field-of-view and can be produced with large detection areas. Their general performance characteristics allow a fair count rate (10^6 Hz/mm^2) and reasonable position resolution (from tens to a few hundred microns). Besides, they can operate at room temperature and are portable and low cost devices, making them desirable for such applications [7, 8].

In this work, the CT system uses a detector based on a Thick-COBRA (THCOBRA), a MPGD which represents an evolution of the MHSP [9]. The same detector was studied in terms of performance characteristics and tested for X-ray transmission imaging, showing good results, presented in ref. [10].

Since the detector was working and operating at its best capabilities at the time of detector performance characterization, its applicability for CT imaging was tested. In this work, it is intended to show the possibility of using a THCOBRA based detector to perform cross-sectional images using X-rays.

The paper is organized as follows: first a description of the CT system is done; in section 3 a description of a simulation study to evaluate the influence of detector discharges, in the CT image is presented as well as the obtained results; in section 4 are shown the cross-sectional and 3D images of a Poly(methyl methacrylate) - PMMA

- phantom filled with different objects and of a sea snail obtained with the CT system. Finally, a discussion and principal conclusions are presented.

2. Experimental Setup

2.1. 2D-THCOBRA description and detector configuration

THCOBRA [9] is a hybrid structure that derives from MHSP [11] and Thick-Gas Electron Multiplier (THGEM) [12], joining the advantages of both structures: intrinsic 2D position discrimination and robustness. The THCOBRA used in the present work, is described in ref.[10] and consists of a 0.4 mm G10 plate coated with a 50 µm Cu layer on both sides. A hole pattern is drilled: each hole has a diameter of 0.3 mm and a rim of 0.08 mm around it. The bottom face of THCOBRA has a pattern of 0.04 mm wide anode strips and 0.2 mm wide cathode strips with a pitch of 1 mm. On the top side of the structure an orthogonal strip pattern is etched to provide the 2D capability. Figure 1a shows a photograph of THCOBRA.

The electrons produced by ionization due to the X-rays interactions with the gas medium are drifted to the THCOBRA structure due to the electric field applied in the drift region (between the detector window and the THCOBRA). A strong electric field inside the holes focus the electrons into them and induces a charge avalanche: the first multiplication stage. The electrons coming from the holes are multiplied again due to the applied voltage between the cathode and anode strips, where the total charge is collected. The operation principle is shown in figure 1b.

The 2D position and energy discrimination of each converted X-ray photon, is determined using a THCOBRA with two resistive lines, orthogonal to each other, a 2D-THCOBRA (figure 1a). One is deposited on the THCOBRA top, connecting the top strips, and the other on the structure bottom connecting the anode strips. Four CANBERRA 2006 preamplifiers integrate the signals generated by each photon interaction, collected at each end of the resistive lines. The four signals are digitized by a CAEN N1728B digitizer with four channels (14 bits Analogue to Digital Converter and 100 MHz of sampling rate) [10]. By measuring the signal amplitude at each end of

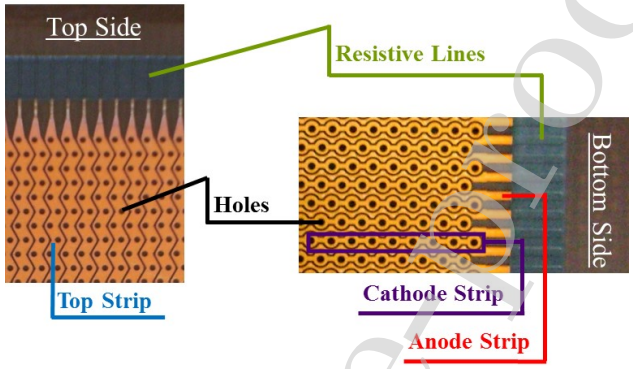

(a)

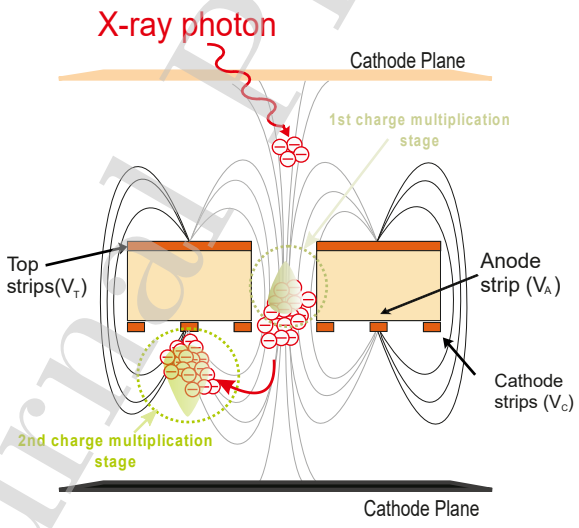

(b)

Figure 1: *(a) Photo of top (left) and bottom (right) faces of THCOBRA structure, showing its electrodes (top, anode and cathode strips), holes and resistive lines [10]; (b) THCOBRA operation principle, showing the two stages of charge multiplication [adapted from [10]].*

the resistive lines and applying the principle of resistive charge division it is possible to determine the X-ray photon position of interaction and energy [13, 14, 15].

The 2D-THCOBRA, with an active area of 10×10 cm^2, was inserted inside the detector chamber and a 1 cm deep drift/absorption region was established. The detector window was made of a 25 μm thick Mylar foil. The electric field of the drift region was set to 350 V/cm. The detector works in a continuous gas flow mode of 25 mL/h of Ne/CH_4 (95/5). The detector performance characterization was previously done (for further details, please see ref. [10]), being the following phase testing the THCOBRA detector for CT imaging.

2.1.1. Gas Choice

The gas medium chosen to fill the detector chamber was $NeCH_4$. Despite $NeCH_4$ is not the first choice gas for imaging applications, since it is a light gas and provides low detection efficiency, the primary reason for its choice is based on the fact that $NeCH_4$ provides high charge gains, increasing the signal to noise-ratio of the measured pulses. As referred, this detector (operating in $NeCH_4$) was characterized in terms of performance characteristics for X-ray imaging in terms of charge gain, energy resolution, stability, count rate capability and spatial resolution. The results of this study showed some good prospects for X-ray imaging applications. However, it is notable the limitation in the spatial resolution (above 1 mm) due the photoelectron range [10, 16, 17]. Nevertheless, it was decided to test the applicability of the detector for CT imaging, since it was already functioning, optimized and very stable.

The strategy to overcome the spatial resolution limitations was to implement image acquisitions with a magnification factor that could compensate for this situation. Therefore, it was established specific distances between the source and detector and between the source and object, in order to achieve a projection image with higher dimensions than the object size.

2.2. Computed Tomography System

Similarly to previous CT systems using MPGDs [6, 18], the CT system, shown in figure 2, is composed by an X-ray tube (Oxford, series 5000), a planar detector and

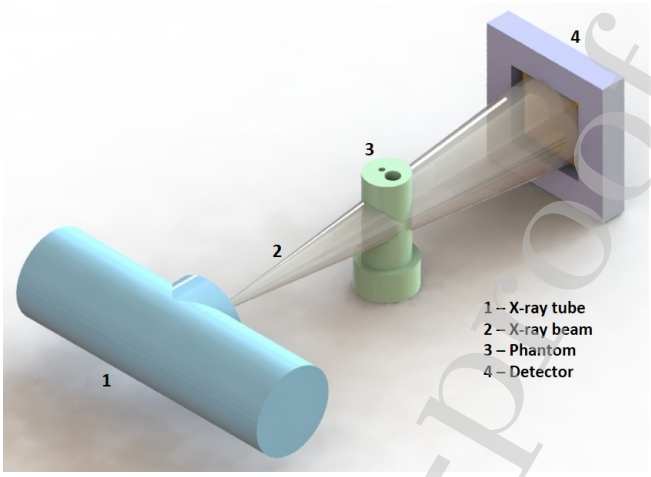

Figure 2: *Sketch of the CT system geometry using a cone X-ray beam and a planar detector.*

a stepper motor which provides the rotation of the object to be imaged. The X-ray tube has a molybdenum anode, it can provide up to 50 kVp and 1 mA, and the X-ray beam was filtered with an aluminum foil of 0.1 mm. The exposition parameters (kVp and mA) were adjusted to each acquisition to meet their requirements .The exposition allowed by the X-ray tube is adequate for the imaged samples herein presented, due to their attenuation coefficients and reduced thicknesses. The source-to-detector and the source-to-object distances were set to 104.5 cm and 22.5 cm, respectively, providing a magnification factor of 4.6. Acquisitions were synchronized with the movement of the stepper motor.

A PMMA phantom and a sea snail were the samples used during the acquisitions presented in this work. The phantom is detailed described in ref.[6] and consists of a cylinder (15 mm of diameter) with two holes. These have a diameter of 5 mm and 2 mm, respectively, a depth of 30 mm and their longitudinal axis parallel to the cylinder axis, allowing to insert a variety of objects. In this work it will be presented images of the phantom with a chalk rod and air filling the biggest and smallest holes, respectively; and with chalk and brass rods in the biggest and smallest holes, respectively.

The presented images were reconstructed using a Matlab® based program that performs filtered reconstruction with the Sheep-Logan filter.

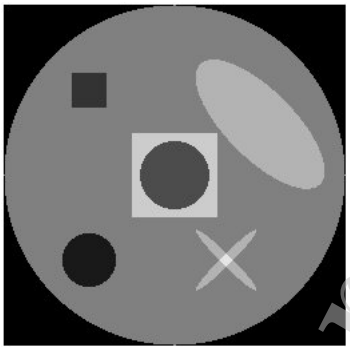

Figure 3: *Matlab® phantom with objects with different shapes (circles, squares and ellipses), some with sharp edges. The objects have also different attenuation coefficients.*

3. Detector Discharges and its influence in the resulting Image

One drawback of the MPGDs technology is the probability of discharges and the consequent recovering time (that can exceed a few seconds) in which no events are recorded and/or their energy can be incorrectly determined (due to the charging up effect that influences pulse height), leading to sinogram inconsistency that can introduce image artefacts [19, 20]. To analyse the influence of discharges on the resulting image, sinograms with discharges were simulated and the respective CT reconstruction was done. The tools used for the simulation do not allow defining the X-ray spectrum or the detector response, however it is still possible to analyse the effect of detector discharges in cross-sectional images.

In a first approach, a general phantom, containing several objects with different shapes and attenuation coefficients, shown in figure 3, was generated using a Matlab® script.

The phantom was used to create two sets of projections consistent with the experimental conditions (for example detector configuration and the number of views): one without and the other with discharges. A linear detector array and 400 views were defined and Poisson noise was added randomly to approximate the simulations to the real experimental conditions.

Discharges were introduced randomly in the sinogram and the influence of the absence of data in some of the views in the reconstructed images was analysed. A

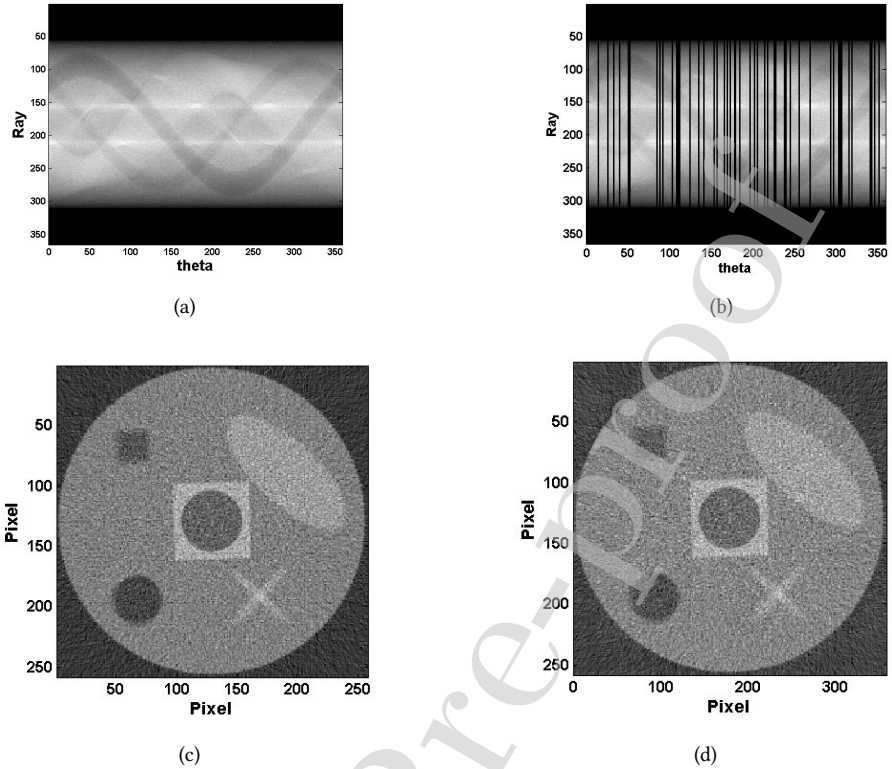

Figure 4: Sinograms without (a) and with (b) discharges, in which "theta" is the angular position of the projetion and "Ray" the ray direction in the projection. (c) and (d): Corresponding cross-sectional images of the respective sinograms.

high discharge frequency in a random pattern was defined in order to approximate the simulation to the experimental condition in which the detector was not stable. The defined discharge frequency for the simulation is much higher than the occurred during the experimental acquisitions herein presented. The cross-sectional images were reconstructed using the parallel geometry algorithm and the results are shown in figure 4.

As can be seen, the CT image reconstructed using the sinogram with discharges does not degrades significantly. The imaged objects are defined and can be clearly distinguished. The SNR was measured in different regions of the image and its variation is not significant, being the maximum difference about only 1%, which means that the image uniformity is not expressively degraded.

To evaluate more specifically the case of the phantom used for experimental acquisitions, the same study was performed using a phantom representing the attenuation coefficients of the PMMA phantom, referred in Section 2.2, also generated by a

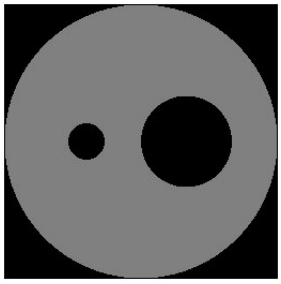

Figure 5: *Matlab® phantom similar to the PMMA phantom used for measurements.*

Matlab® cript, considering that there are no objects filling the holes. An image of the generated phantom is shown in figure 5.

The cross-sectional images were reconstructed using the parallel geometry algorithm and the results are shown in figure 6

The reconstructed images of figure 6 are an example of the expected images using the PMMA phantom. The constituents of the image are defined and can be clearly distinguished. It seems that the discharges do not influence the image quality significantly and the SNR degradation in this case has an average value of about only 2%. In order to allow a quantitative analysis and a comparison between the simulation and experimental images of this work further in the document, the contrast and Contrast-to-Noise Ratio (CNR) between the smaller rod and the PMMA were calculated, being, respectively, 30% and 2,3.

4. CT Imaging

Three examples of CT imaging studies are presented: the PMMA phantom filled with chalk and air; the PMMA phantom with chalk and brass and a sea snail. Cross-sectional and tri-dimensional (3D) images are presented in the next subsections. Photographs of the imaged objects can be seen in figure 7.

4.1. PMMA Phantom with chalk and air

The PMMA phantom with chalk and air was imaged with an X-ray tube voltage and current of 25 kVp and 18 μA, respectively, which resulted in a detection rate of 2,6

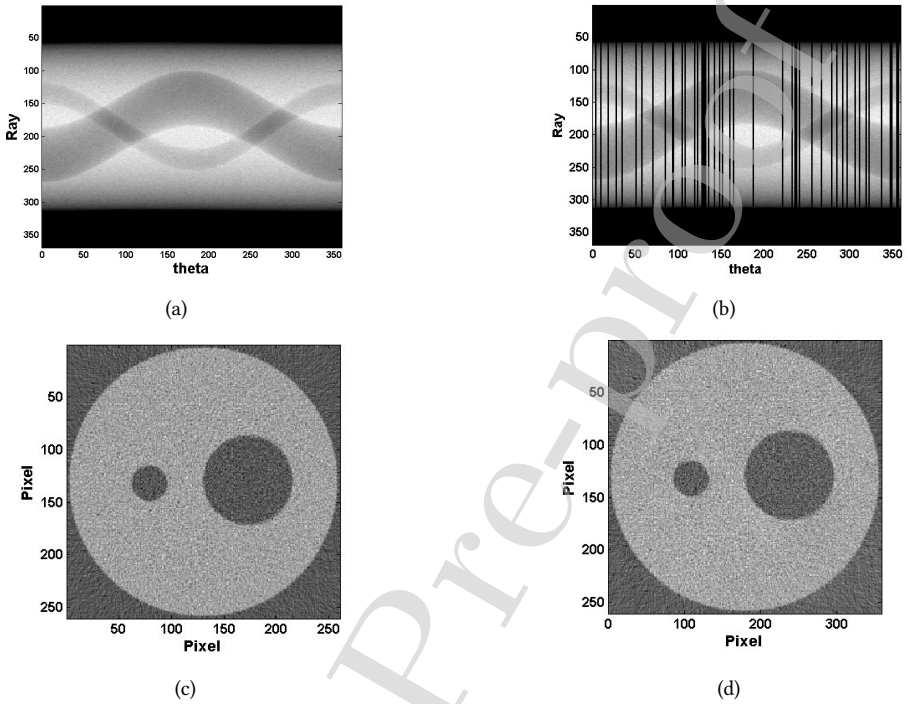

Figure 6: Sinograms without (a) and with (b) discharges. (c) and (d): Reconstructed images using the respective sinograms.

Figure 7: Photos of the imaged objects: (a) PMMA phantom with chalk and brass filling its holes (b) sea snail.

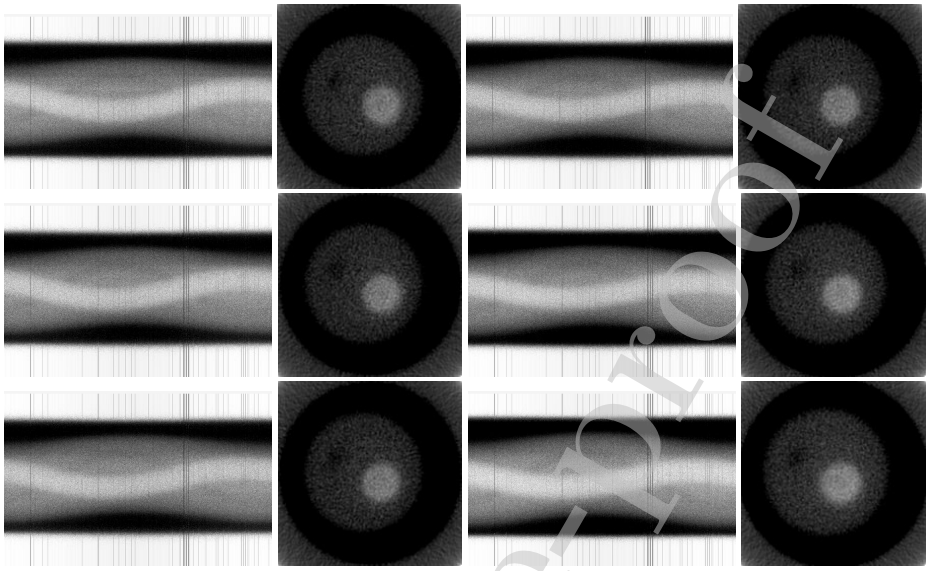

Figure 8: Sinograms of the PMMA phantom with chalk and air (left) and the corresponding cross-sectional images (on the sinograms right)(Please see video 1 - PMMAChalkAir).

$\times 10^4$ events per second. 400 views with an acquisition time of 7 s each were stored, resulting in a total acquisition time of 47 min. The data was organized in six sinograms and the respective cross-sectional images were reconstructed, both shown in figure 8 (for animation of cross-sectional images, please see video 1 - PMMAChalkAir). The cross-sectional images were reconstructed with 190×190 pixels using sinograms with 256 rays. Each cross-sectional image corresponds to an object section of 2.8 mm.

In the sinograms of figure 8 the chalk rod and the PMMA phantom can be clearly distinguished and with good contrast. Although the air rod has lower contrast, it can be also seen in all the cross sectional images.

For this experimental acquisition it was calculated the contrast and CNR between the air rod and the PMMA phantom, achieving about 42% and 1,5, respectively. Comparing with the values obtained for the simulated image of the PMMA phantom, the experimental image reaches an higher contrast, however, this measure does not consider the noise present in the image, visibly higher than the simulated image. CNR takes noise into account being, as expected, 28% higher in the simulated image.

The presented cross-sectional images were stacked up to compute a 3D image of

the corresponding section of the PMMA phantom. Then, to visualize a specific surface, a window of values representative of that surface was selected and the corresponding iso-surface is shown. To represent the object surfaces, the corresponding window values for PMMA, chalk and air surfaces were defined. The resulting image is shown in figure 9.

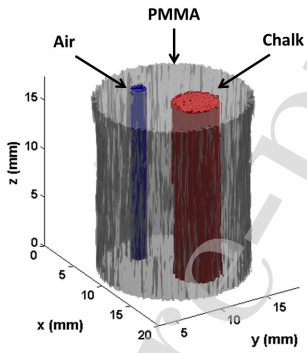

Figure 9: 3D image of the PMMA phantom with chalk and air, in which the PMMA surface is represented in gray, the chalk surface in red and the air surface in blue.

Despite some artefacts, the 3D image of the phantom with chalk and air shows the three surfaces. The most well defined surface is the one corresponding to the chalk rod with less surrounding structures with the same isovalue. The air rod and the PMMA are also well defined, however with more irregularities in their surfaces. Nevertheless, the image can represent the imaged object: the phantom with approximately 15 mm of diameter and the chalk and air rods, respectively with 2 mm and 5 mm, are correctly represented in the image.

Taking advantage of the spectral capabilities of the THCOBRA detector, images using partial ranges of the spectrum were reconstructed, being shown in figure 10. Three images using low, medium and high energies of the spectrum were reconstructed and the image using the entire spectrum was included to facilitate a comparison.

The image using the lowest energy range (figure 10c) presents some noise and the contrast between the chalk and PMMA is significantly reduced when compared

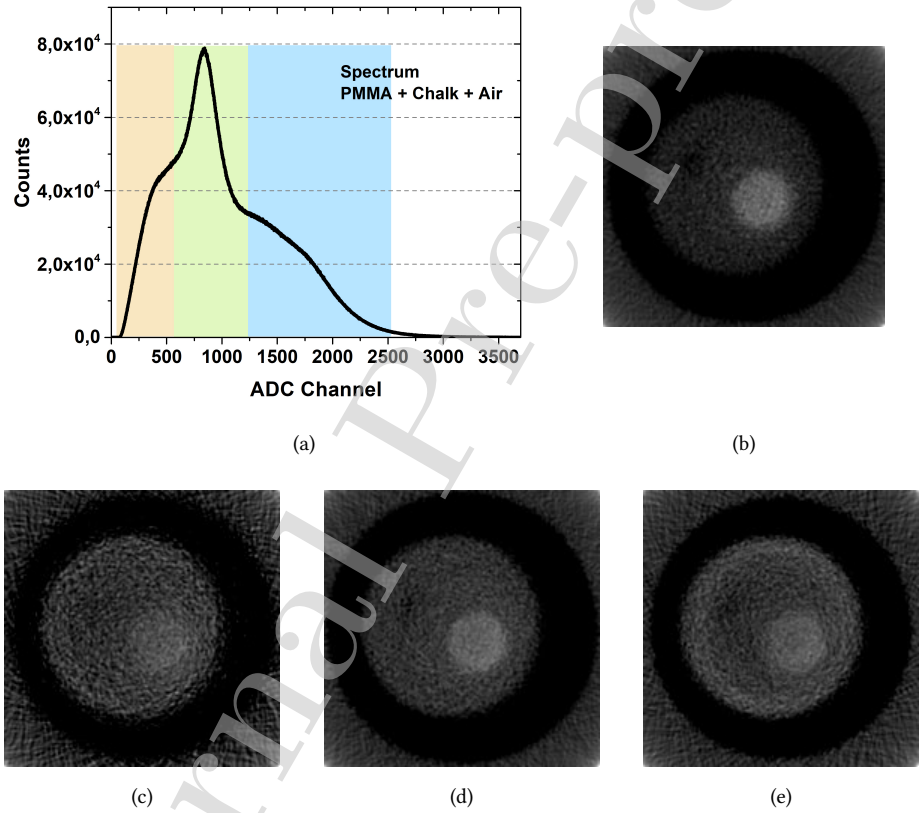

Figure 10: (a) Spectrum of PMMA with chalk and air acquisition, showing the energy ranges (low in orange, medium in green and high in blue) used to reconstruct different cross-sectional images. Cross-sectional images reconstruction using: (b) full spectrum, (c) low energies (d) medium energies and (e) high energies.

with all the other images. In this image, the region corresponding to the air is not distinguishable from the PMMA, being the PMMA is in evidence in this image. The medium energy image (figure 10d) allows the discrimination of the air region and provides a good contrast between the chalk rod and the PMMA. Figure 10d shows the PMMA better than the others and is a smother image. The highest energy image (figure 10e) shows more evidently beam artefacts characterized by the low intensity region in the centre of the phantom. Concerning CNR (between the chalk rod and the PMMA), figure 10c has the lowest value, while the image considering medium energies (figure 10d) has the highest value, which was expected from the qualitative analysis. Comparatively to the image reconstructed with full spectrum, all have lower CNR at least 50%, which is related with the noise increase due to lower statistics, and in the case of figure 10d contributes the lower contrast between the chalk and the PMMA.

4.2. PMMA Phantom with chalk and brass

The PMMA phantom with chalk and brass was irradiated also with an X-ray tube voltage and current of 25 kVp and 18 μA, respectively, to acquire 400 views, each with an acquisition time of 7 s. The detection rate was similar to the previous example (2,6 $\times$ 10^4). 10 CT images were reconstructed with 190 $\times$ 190 pixels using sinograms with 256 rays, each corresponding to a cross-section of 1.7 mm. The resulting images are shown in figure 11 (please see video 2 - PMMAChalkBrass for animation of cross-sectional images).

The sinograms show the structures of the imaged components (PMMA, chalk and brass) with a good contrast and it is possible to distinguish them very well. The cross-sectional images, similarly to the sinograms, show all the components well distinguished with a good contrast. The improved discrimination of objects comparatively to the previous case can be explained by the high contrast between the components, due to its higher attenuation coefficients. Also, beam hardening artefacts are visible between the chalk and brass rod and in the external area of the phantom near the brass rod.

Contrast and CNR were measured between the the chalk rod and the PMMA and

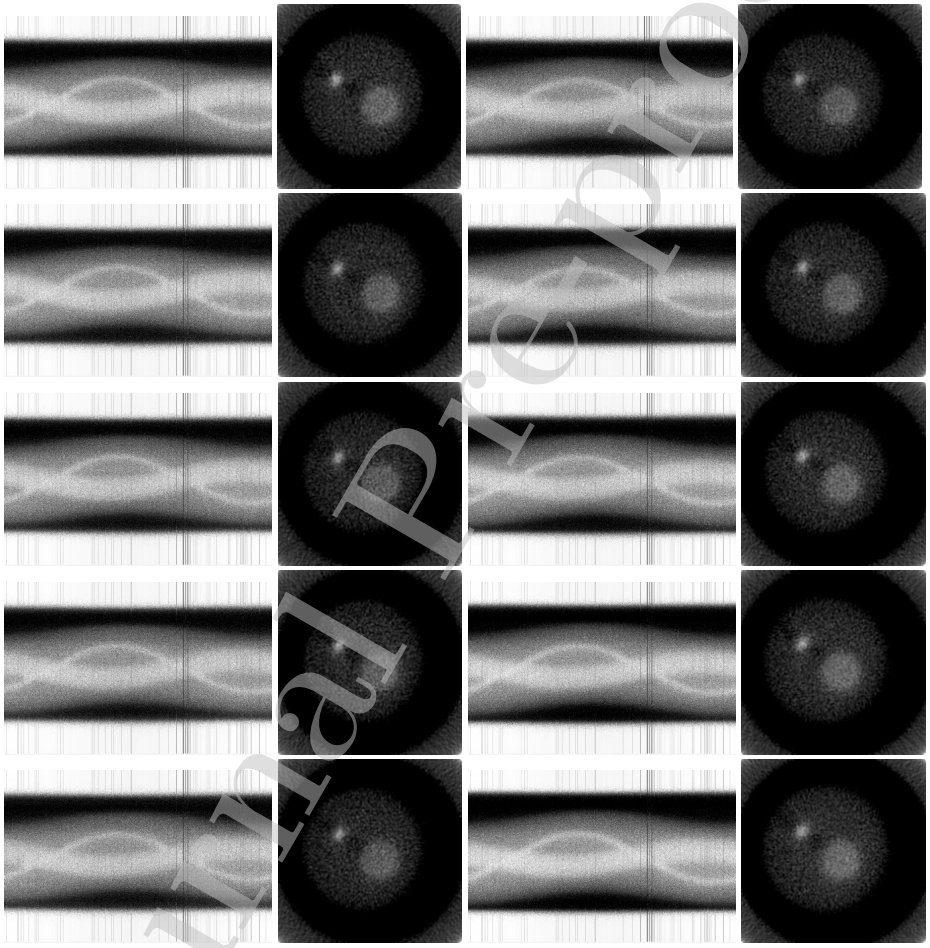

Figure 11: Sinograms of the PMMA phantom with chalk and brass (left) and the corresponding cross-sectional images (on the sinograms right)(Please see video 2 - PMMAChalkBrass).

between the brass rod and the PMMA. Concerning the contrast were achieved 42% between the chalk rod and the PMMA and 56% between the brass rod and the PMMA. The CNR was 3,4 and 4,7, respectively. The higher values, when compared with the previous example, are related essentially, to the higher contrast in this case.

The 3D image was reconstructed using the slices shown in figure 11. In the 3D image of figure 12 the chalk and brass rods are clearly distinguished from each other and from the PMMA. Since a good contrast in the cross-sectional images was presented, the selection of the surfaces isovalues was easier than in the previous case. It is interesting to note that the beam hardening artefact is also visible in the 3D image: in the external area of the PMMA near the brass rod there is a lower intensity region due to this artefact.

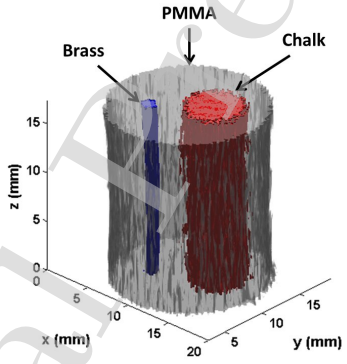

Figure 12: 3D image of the phantom with chalk and brass, in which the PMMA surface is represented in gray, the chalk surface in red and the brass surface in blue.

In this case, cross-sectional images using energy ranges from the spectrum were also reconstructed (figure 13), using the same methodology of the previous case.

The object with more representation in the image using the lowest energy range (figure 13c) is the PMMA, while the other components (chalk and brass), despite being distinguishable, have almost no contrast. In the medium energy image (figure 13d) the components have a good contrast between them and compared to the full energy image (figure 13b), the PMMA is more visible. The image that considers the highest energies is noisier and shows, once again, more clearly artefacts of beam hardening.

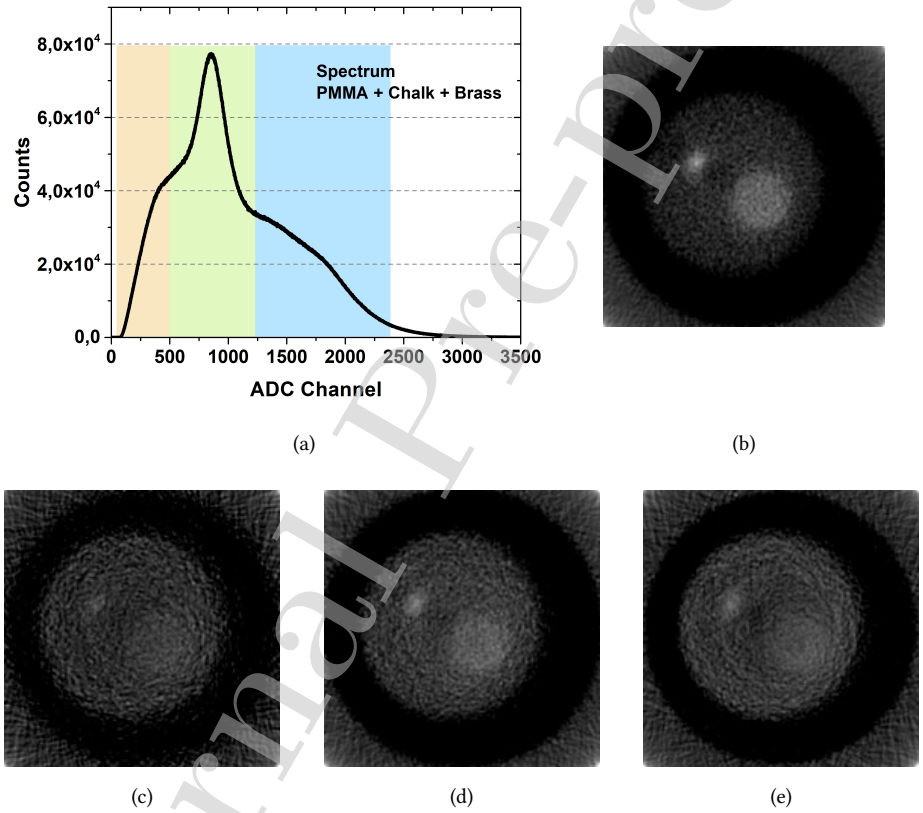

Figure 13: (a) Spectrum of PMMA with chalk and air acquisition, showing the energy ranges (low in orange, medium in green and high in blue) used to reconstruct different cross-sectional images. Cross-sectional images reconstruction using: (b) full spectrum, (c) low energies (d) medium energies and (e) high energies.

The contrast between the chalk and PMMA is higher in the full energy image, followed by the medium energy image. CNR follows the same behaviour and is only about 45% of the CNR value of the original image (complete spectrum). The image reconstructed using low energy ranges has the lowest CNR, followed by the high energy image. The results are in accordance with the qualitative analysis.

4.3. Sea snail

A sea snail was also used for CT imaging. The X-ray tube voltage and current were set to 50 kVp and 6 μA, respectively, to acquire 400 views, each with 10 s of acquisition time. The X-ray tube voltage was increased compared to the previous examples, to generate photons with energy adequate for provide differential contrast of the sea snail shell. In this case, the detection rate was about $2{,}8 \times 10^4$. 15 sinograms and the respective cross-sectional images were obtained and are shown in figure 14 (animation of cross-sectional images shown in video 3 - SeaSnail). The sea snail has a height of 2 cm, which means that each cross-sectional image corresponds to a slice in the object of approximately 1.3 mm (for the specified magnification factor).

Some structures of the sea snail can be distinguished in the sinogram, as for example the central axis which is denser. The cross-sectional anatomy of the sample is well visible in the cross-sectional images. The sea snail exoskeleton is clearly visible from the bottom up to the apex. Its internal space reduces from the columella up to the apex, which is also demonstrated in the CT images. In the cross-sectional images corresponding to the upper part of the sea snail, some partial volume effect is visible. Generally, the perceptual image quality is good taking into account the slice thickness. The CT images represent truthfully the sea snail, showing its exoskeleton with good definition and contrast.

Using the presented cross-sectional images, a 3D image was computed. Figure 15 shows the obtained images, in which different perspectives of the sample are visible.

In the front perspective (figure 15a) in the left middle area of the volume, a part of the shell is not visible, because a small area is out of the field of view. This is consistent with the cross-sectional images of figure 14, in which the shell is not completely visible. In this image, the sea snail aperture is clearly visible. In the back perspective

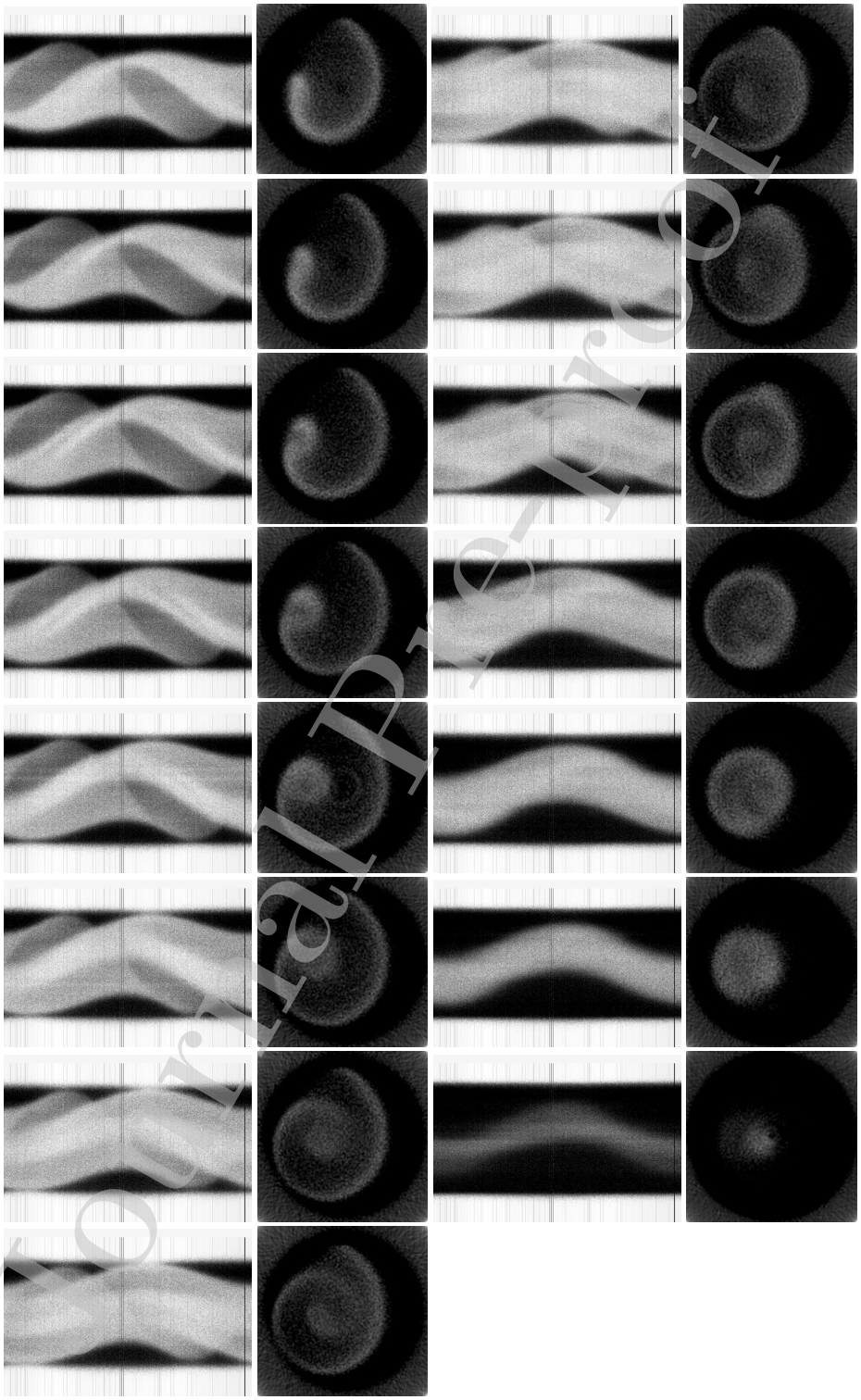

Figure 14: Sea snail sinograms (left) and the corresponding cross-sectional images (on the sinograms right)(Please see video 3 - SeaSnail).

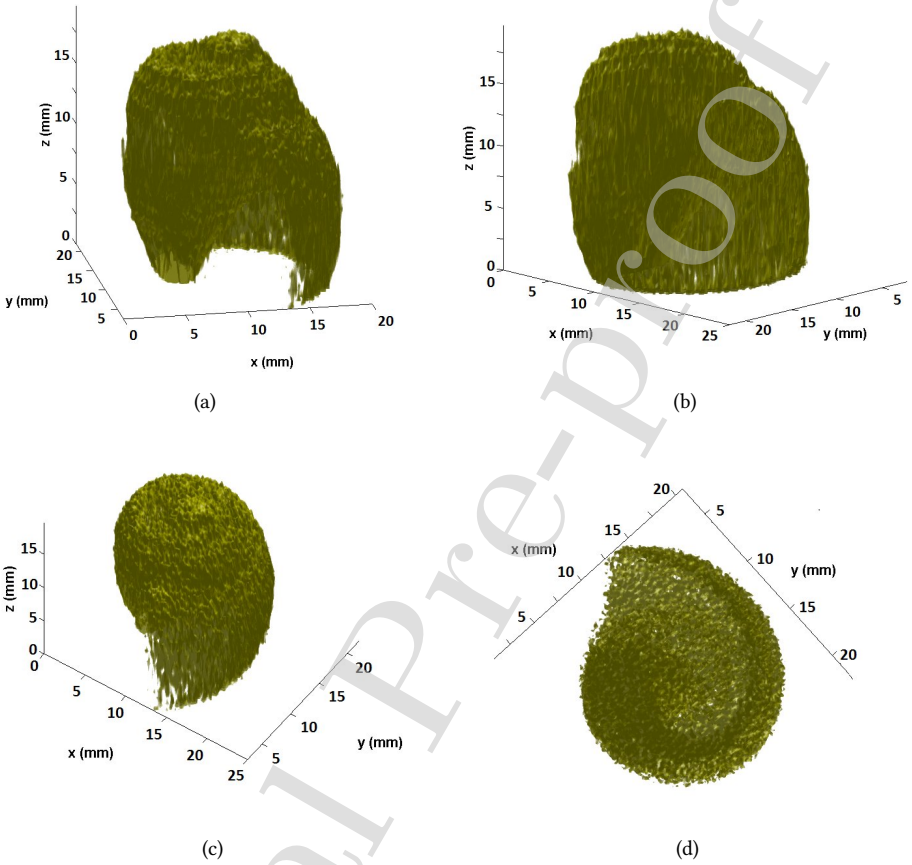

Figure 15: 3D image of the sea snail computed using the 15 cross-sectional images. Front (a), back (b), oblique (c) and bottom (d) perspectives are shown.

of the 3D image (figure 15b) the sea snail back is truthfully represented. The oblique perspective (figure 15c) shows the sutures which and can be distinguished from the remaining shell. Finally, in the bottom perspective (figure 15d), the interior cavity filled with air is also clearly visible.

A good representation of the sea snail was achieved. The contours can be defined and separated from the air regions.

The sea snail imaging is considered a successful example using the developed detector, clearly visualizing the sea snail exoskeleton with good contrast and definition. In the future it is intended to apply post-processing to the images, which is expected

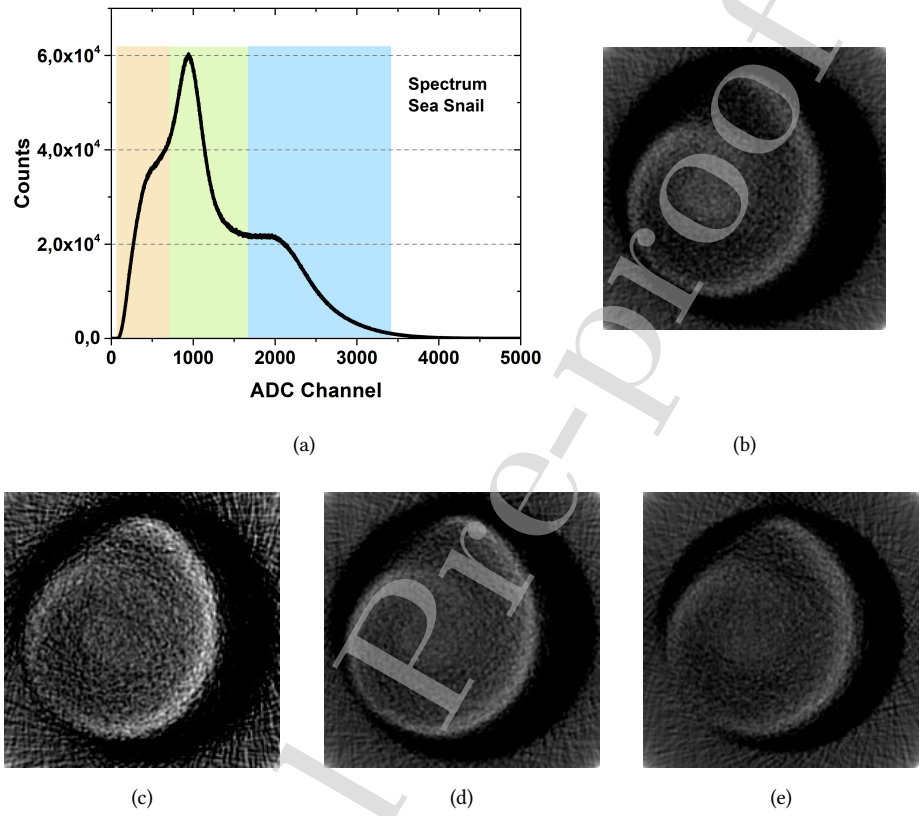

Figure 16: (a) Spectrum of PMMA with chalk and air acquisition, showing the energy ranges (low in orange, medium in green and high in blue) used to reconstruct different cross-sectional images. Cross-sectional images reconstruction using: (b) full spectrum, (c) low energies (d) medium energies and (e) high energies.

to enhance image quality significantly.

Figure 16 shows the acquisition spectrum and cross-sectional images of a middle section of the sea snail reconstructed with different energy ranges, similarly to the previous cases.

Concerning the partial energy reconstructions of the sea snail, the middle energy image (figure 16d) is the one that presents better definition of contours and less noise. The lowest energy image (figure 16c) is the noisiest. In the image that considered the highest energies (figure 16e), the contours of the sea snail shell have less contrast

than in figure 16d. In this case, contrast and CNR were not calculated, since that a selection of a region of interest in the sea snail shell would have a small very area and be strongly affected by the noise.

4.4. Filling gas and Image Quality

The presented images, acquired with a magnification factor of 4.6, can represent the irradiated object. The applied magnification factor allowed to identify the object structures and up to some point compensate for the spatial resolution limitation arisen from the gas medium and even so it was possible to reconstruct a 3D image of the sea snail with reliability.

Besides the high photoelectron range, that influences spatial resolution, $NeCH_4$ has lower detection efficiency for X-ray detection when compared to other gas mediums, such as krypton or xenon. For instance, the difference between the detection efficiencies of $NeCH_4$ and pure krypton is about one order of magnitude for low energy photons and two orders of magnitude for photons energies above approximately 15 keV, as shown in figure 17. $ArCH_4$ is also shown, allowing to verify that its detection efficiency is still lower than xenon or krypton about one order of magnitude.

Concerning the above, noble gases with higher atomic number, such as krypton, were considered [21], to improve both the detection efficiency and position resolution. In the future, mixtures of xenon and krypton will be tested in order to maximize these parameters in an energy range up to approximately 35 keV. The goal of these studies is the development a low cost X-ray computed tomography imaging system for breast and small animal studies, which require photon energies in the range of highest detection efficiency.

5. Discussion and Conclusions

Gaseous detectors present lower density than solid state detectors, which leads to lower detection efficiency and spatial resolution. Therefore, it is not expected to achieve the same panorama for some performance characteristics. However, as stated, gaseous detectors have a considerably lower cost and can be developed in large active

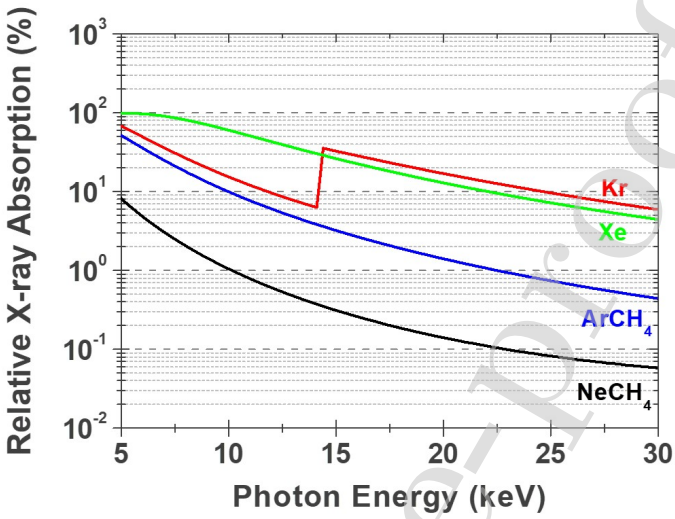

Figure 17: Relative X-ray absorption as a function of photon energy for $NeCH_4$, $ArCH_4$, pure Xe and pure Kr at 1 bar.

areas without dead zones, which make them interesting for application in some fields such as small animal imaging in biomedical studies and breast imaging. Particularly, THCOBRA, when compared to other MPGDs allows high charge gains due to the two charge multiplication stages in a single structure and provides intrinsic position and energy discrimination, which gives a good signal-to-noise ratio of the pulses while simplifies the detector development.

The detector performance is extremely dependent on the gas, which dictates physical phenomena. This study and the previous [10] show that $NeCH_4$ present some limitations for X-ray imaging, particularly detection efficiency and spatial resolution. Despite this, the strategy to overcome the spatial resolution limited by the gas medium (consisting of magnifying the projection image) allowed achieve cross-sectional images with reasonable representation of the imaged objects. Concerning the reduced detection efficiency, it can be surpassed by increasing the acquisition time, which in this case, does not represents a problem (the dose considerations for a living being do not apply). Other parameters such as energy resolution or charge gain are comparable

to THGEM detectors. Energy resolution of THCOBRA (about 22% FWHM at 8 keV [10]) and THGEM (30% FWHM at 5.9 keV [16]) are similar, and the charge gain of THCOBRA is comparable of a double THGEM detector (with a more complex development). The stability of the presented detector, providing good signal-to-noise ratio of pulses for relatively low applied voltages [10], allowed to perform this viability study for CT imaging.

The simulation study, despite of its limitations, shows that image quality does not degrade significantly due to detector discharges. In the future, parameters such as the energy spectrum will be considered.

The presented CT system used for the first time a MPGD with an active area of 10×10 cm^2 turning possible a magnification factor of 4.6, allowing a more detailed X-ray CT image of the studied objects. This is of significant importance, since the characterization study of this detector showed a limitation in the spatial resolution associated with the gas medium [10].

In the case of the PMMA phantom all the objects could be distinguished both in cross-sectional and 3D images. In images of the PMMA phantom with chalk and air, although the air region could be seen its contours are not perfectly defined; on the other hand, in the PMMA phantom with chalk and brass images, all the components were completely defined.

The sea snail images are an example of a successful application of the 2D-THCOBRA detector for CT imaging. The sea snail is truthfully represented both in cross-sectional and 3D images, its main structures are visible and can be identified.

Reconstructions of partial energy cross-sectional images were performed, enhancing different components depending on the selected energy interval. Despite these differences, it is common the increase of noise in the lowest energy ranges, followed by the highest energy ranges. The smoothest image in all the cases is the one using medium energies, which presents also the best CNR among the three. For comparison, the middle energy images can represent the PMMA more highlighted than the image using the complete spectrum and in all the cases present a CNR lower than the full spectrum images.

Although the obtained images do not have post processing, they already shown

the imaged object and image quality which can probably be enhanced, particularly in the contrast, contour definition and noise reduction, which is intended for the future.

Also, image quality can be improved using other filling gases in the detector chamber that maximizes both absorption efficiency and spatial resolution. $NeCH_4$ (95/5) have limited position resolutions and detection efficiency for x-ray energies above about 10 keV, being mandatory the use of heavier noble gases for image quality improvements [17]. Heavier noble gases, such as pure Kr, pure Xe or mixtures, could be an adequate choice [17] and will be considered in future works. Presently, pure Kr is being studied, having already shown good prospects for this kind of applications [17, 21].

Acknowledgments

The costs resulting from the FCT - Fundação para a Ciência e a Tecnologia, I.P hiring L. F. N. D. Carramate is funded by national funds (OE), in the scope of the framework contract CEECIND/01369/2017. The costs resulting from the FCT hiring of C. D. R. Azevedo is funded by OE, through FCT, in the scope of the framework contract foreseen in the numbers 4, 5 and 6 of the article 23, of the Decree-Law 57/2016, of August 29, changed by Law 57/2017, of July 19. This work was partially supported by projects UID/CTM/50025/2019, PTDC/FIS-AQM/32536/2017 and CERN/FIS-INS/0025/2017 through COMPETE, FEDER and FCT programs.

References

References

[1] T. M. Buzug, Computed Tomography: from Photon Statistics to Modern Cone-Beam CT, Springer-Verlag, 2008. doi:10.1007/978-3-540-39408-2.

[2] J. Hsieh, Computed tomography: principles, design, artifacts, and recent advances, 2nd Edition, SPIE & Jonh Wiley& Sons, Inc., 2009.
URL http://ebooks.spiedigitallibrary.org/book.aspx?bookid=92

[3] J. Giersch, D. Niederlöhner, G. Anton, The influence of energy weighting on X-ray imaging quality, Nuclear Instruments and Methods in Physics Research Section A: Accelerators, Spectrometers, Detectors and Associated Equipment 531 (2004) 68–74. doi:10.1016/j.nima.2004.05.076.

[4] C. A. B. Oliveira, C. A. Santos, L. F. Carramate, A. L. M. Silva, N. da Luz, J. M. F. dos Santos, J. F. C. A. Veloso, Energy Weighting in a 2D-MHSP X-Ray Single Photon Detector, IEEE Transactions on Nuclear Science 57 (3) (2010) 938–943. doi:10.1109/TNS.2010.2044806.

[5] P. M. Shikhaliev, Energy-resolved computed tomography: first experimental results., Physics in medicine and biology 53 (20) (2008) 5595–613. doi:10.1088/0031-9155/53/20/002.
URL http://www.ncbi.nlm.nih.gov/pubmed/18799830

[6] L. F. N. D. Carramate, C. A. B. Oliveira, A. L. M. Silva, A. M. D. Silva, J. M. F. D. Santos, J. F. C. A. Veloso, Energy weighting technique in Quantum Computed Tomography using a MPGD, Journal of Instrumentation 6 (02) (2011) C02002. doi:10.1088/1748-0221/6/02/C02002.
URL http://stacks.iop.org/1748-0221/6/i=02/a=C02002?key=crossref.b635fd46eee04ea6df312983a0ea4c09

[7] G. Steinhauser, K. Buchtela, Handbook of Radioactivity Analysis, third edit Edition, Elsevier, Vienna, 2012. doi:10.1016/B978-0-12-384873-4.00003-7.
URL http://dx.doi.org/10.1016/B978-0-12-384873-4.00003-7

[8] G. F. Knoll, Radiation detection and measurement, 4th Edition, Jonh Wiley & Sons, Inc, Ann Arbor, 2010.
URL http://books.google.com/books?hl=en{&}lr={&}id=4vTJ7UDel5IC{&}oi=fnd{&}pg=PA1{&}dq=Radiation+detection+and+measurement{&}ots=VuGVCPxKdC{&}sig=ztKzy35h5Smi7m99nQuT59yU0AE

[9] F. D. Amaro, C. Santos, J. F. C. A. Veloso, A. Breskin, R. Chechik, J. M. F. D. Santos, The Thick-COBRA: a new gaseous electron multiplier for radiation detectors, Journal of Instrumentation 5 (10) (2010) P10002. doi:10.1088/1748-0221/5/10/P10002.
URL http://stacks.iop.org/1748-0221/5/i=10/a=P10002?key=crossref.da978431938d7b9fdf90ae142d2c7479

[10] L. F. N. D. Carramate, A. L. M. Silva, C. D. R. Azevedo, D. S. Covita, J. F. C. A. Veloso, THCOBRA X-ray imaging detector operating in Ne/CH 4, Journal of Instrumentation 10 (01) (2015) P01003–P01003. doi:10.1088/1748-0221/10/01/P01003.
URL http://stacks.iop.org/1748-0221/10/i=01/a=P01003

[11] J. F. C. A. Veloso, J. M. F. dos Santos, C. A. N. Conde, A proposed new microstructure for gas radiation detectors: The microhole and strip plate, Review of Scientific Instruments 71 (6) (2000) 2371–2376. doi:10.1063/1.1150623.

[12] R. Chechik, A. Breskin, C. Shalem, D. Mörmann, Thick GEM-like hole multipliers: properties and possible applications, Nuclear Instruments and Methods in Physics Research Section A: Accelerators, Spectrometers, Detectors and Associated Equipment 535 (1-2) (2004) 303–308. doi:10.1016/j.nima.2004.07.138.
URL http://linkinghub.elsevier.com/retrieve/pii/S0168900204016663

[13] H. Natal da Luz, J. Veloso, J. dos Santos, J. A. Mir, A simple X-ray position detection system based on a MHSP, Nuclear Instruments and Methods in Physics Research Section A: Accelerators, Spectrometers, Detectors and Associated Equipment 580 (2) (2007) 1083–1086. doi:10.1016/j.nima.2007.06.083.
URL http://linkinghub.elsevier.com/retrieve/pii/S0168900207013289

[14] H. Natal da Luz, J. Veloso, N. Mendes, J. dos Santos, J. Mir, MHSP with position

detection capability, Nuclear Instruments and Methods in Physics Research Section A: Accelerators, Spectrometers, Detectors and Associated Equipment 573 (1-2) (2007) 191–194. doi:10.1016/j.nima.2006.10.243.
URL http://linkinghub.elsevier.com/retrieve/pii/S0168900206021668

[15] A. L. M. Silva, C. D. R. Azevedo, L. F. N. D. Carramate, T. Lopes, I. F. Castro, R. D. Oliveira, J. F. C. A. Veloso, X-ray imaging detector based on a position sensitive THCOBRA with resistive line, Journal of Instrumentation 8 (05) (2013) P05016–P05016. doi:10.1088/1748-0221/8/05/P05016.
URL http://stacks.iop.org/1748-0221/8/i=05/a=P05016?key=crossref.5edb203a7fc315d077b1e1a7c4b6137b

[16] M. Cortesi, V. Peskov, G. Bartesaghi, J. Miyamoto, S. Cohen, R. Chechik, J. M. Maia, G. Gambarini, V. Dangendorf, A. Breskin, THGEM operation in Ne and Ne / CH 4, Journal of Instrumentation (4 P08001). doi:10.1088/1748-0221/4/08/P08001.

[17] C. Azevedo, S. Biagi, R. Veenhof, P. Correia, A. Silva, L. Carramate, J. Veloso, Position resolution limits in pure noble gaseous detectors for X-ray energies from 1 to 60 keV, Physics Letters B 741 (2015) 272–275. doi:10.1016/j.physletb.2014.12.054.
URL http://www.sciencedirect.com/science/article/pii/S0370269314009356

[18] L. F. N. D. Carramate, C. A. B. Oliveira, A. L. M. Silva, A. M. D. Silva, J. M. F. D. Santos, J. F. C. A. Veloso, Multi-slice quantum Computed Tomography system using a MHSP, Journal of Instrumentation 7 (01) (2012) C01106–C01106. doi:10.1088/1748-0221/7/01/C01106.
URL http://stacks.iop.org/1748-0221/7/i=01/a=C01106?key=crossref.9db67d65297d5469529ee5bba3171ee3

[19] J. Xu, K. Taguchi, B. M. W. Tsui, Statistical projection completion in X-ray CT using consistency conditions., IEEE transactions on medical imaging 29 (8)

(2010) 1528–40. doi:10.1109/TMI.2010.2048335.
URL http://www.pubmedcentral.nih.gov/articlerender.fcgi?artid=3097419{&}tool=pmcentrez{&}rendertype=abstract

[20] G.-H. Chen, S. Leng, A new data consistency condition for fan-beam projection data, Medical Physics 32 (4) (2005) 961. doi:10.1118/1.1861395.
URL http://scitation.aip.org/content/aapm/journal/medphys/32/4/10.1118/1.1861395

[21] L. F. N. D. Carramate, A. L. M. Silva, C. D. R. Azevedo, I. Fortes, S. G. Monteiro, S. Sousa, F. M. Ribeiro, S. De Francesco, D. S. Covita, J. F. C. A. Veloso, THCOBRA X-ray imaging detector operating in pure Kr, Journal of Instrumentation 12 (05) (2017) T05003. doi:10.1088/1748-0221/12/05/T05003.